Atmos. Chem. Phys., 15, 3815–3829, 2015
www.atmos-chem-phys.net/15/3815/2015/
doi:10.5194/acp-15-3815-2015

Atmospheric Chemistry and Physics
Open Access

CCN activation of fumed silica aerosols mixed with soluble pollutants

M. Dalirian[1], H. Keskinen[2,3], L. Ahlm[1], A. Ylisirniö[2], S. Romakkaniemi[2,5], A. Laaksonen[2,4], A. Virtanen[2], and I. Riipinen[1]

[1]Department of Environmental Science and Analytical Chemistry (ACES) and the Bolin Centre for Climate research, Stockholm University, Stockholm, Sweden
[2]Department of Applied Physics, University of Eastern Finland, Kuopio, Finland
[3]Department of Physics, University of Helsinki, Helsinki, Finland
[4]Finnish Meteorological Institute, Helsinki, Finland
[5]Finnish Meteorological Institute, Kuopio, Finland

Correspondence to: M. Dalirian (maryam.dalirian@aces.su.se)

Received: 13 June 2014 – Published in Atmos. Chem. Phys. Discuss.: 8 September 2014
Revised: 11 February 2015 – Accepted: 21 February 2015 – Published: 9 April 2015

Abstract. Particle–water interactions of completely soluble or insoluble particles are fairly well understood but less is known of aerosols consisting of mixtures of soluble and insoluble components. In this study, laboratory measurements were performed to investigate cloud condensation nuclei (CCN) activity of silica particles mixed with ammonium sulfate (a salt), sucrose (a sugar) and bovine serum albumin known as BSA (a protein). The agglomerated structure of the silica particles was investigated using measurements with a differential mobility analyser (DMA) and an aerosol particle mass analyser (APM). Based on these data, the particles were assumed to be compact agglomerates when studying their CCN activation capabilities. Furthermore, the critical supersaturations of particles consisting of pure and mixed soluble and insoluble compounds were explored using existing theoretical frameworks. These results showed that the CCN activation of single-component particles was in good agreement with Köhler- and adsorption theory based models when the agglomerated structure was accounted for. For mixed particles the CCN activation was governed by the soluble components, and the soluble fraction varied considerably with particle size for our wet-generated aerosols. Our results confirm the hypothesis that knowing the soluble fraction is the key parameter needed for describing the CCN activation of mixed aerosols, and highlight the importance of controlled coating techniques for acquiring a detailed understanding of the CCN activation of atmospheric insoluble particles mixed with soluble pollutants.

1 Introduction

The atmosphere of the Earth is composed of gases and suspended liquid and solid aerosol particles of different size, shape and chemical composition. Atmospheric aerosols have several important impacts on the environment. First, at high concentrations in urban areas, they are a health hazard to the respiratory system causing millions of premature deaths every year (Mackay and Mensah, 2004; Pope and Dockery, 2006; Pope et al., 2009). Second, they scatter and absorb solar and thermal radiation and thereby directly influence the heat balance of the Earth and thus the climate (McCormick and Ludwig, 1976; Haywood and Boucher, 2000; Ramanathan et al., 2001) Third, they act as cloud condensation nuclei (CCN) and ice nuclei (IN). Hence, they alter the microphysical properties of clouds and thereby indirectly affect the climate (Twomey, 1974; Albrecht, 1989; Lohmann and Feichter, 2005). Fourth, atmospheric surface and condensed-phase chemistry can occur in the aerosol phase (Ravishankara, 1997; Seinfeld and Pandis, 2006).

Aerosol–cloud interactions represent the largest uncertainty in predictions of the future climate (IPCC, 2013). To reduce this uncertainty we need to improve our understanding of the activation of aerosol particles to cloud droplets. In general, the ability of aerosol particles to act as CCN depends on their composition, size and structure (Kumar et al., 2011a). Besides soluble aerosol particles, insoluble particles like soot, mineral dust and silica can act as CCN – particu-

larly if they are coated with hygroscopic material (Kumar et al., 2009).

During atmospheric transport and aging, originally insoluble particles may acquire soluble species like $(NH_4)_2SO_4$ (ammonium sulfate) on their surfaces (Levin et al., 1996). In such cases, the threshold supersaturation of cloud droplet activation substantially decreases when water adsorbs onto the slightly soluble particles giving rise to the process of adsorption activation (Saathoff et al., 2003; Hings et al., 2008). Thus, the presence of soluble species on insoluble particle surfaces can enhance water–particle interactions and CCN activity of the particles. Several recent studies have focused on the CCN activation of insoluble and mixed soluble–insoluble particles, leading to the development of new theoretical frameworks for describing the relevant phenomena. The developed theories are often based on multilayer adsorption models and account for the curvature effects of the particles. One of these theories introduced by Sorjamaa and Laaksonen (2007) combined FHH (Frenkel, Halsey and Hill) adsorption isotherms and traditional Köhler theory to describe the equilibrium growth of insoluble particles. Sorjamaa and Laaksonen (2007) showed that adsorption could help wettable insoluble compounds to activate in the atmosphere. Thereafter, Kumar et al. (2009) developed a cloud droplet formation parametrization in which the CCN constitute an external mixture of soluble aerosol, that follows Köhler theory, and insoluble aerosol, that follows FHH adsorption activation theory (FHH-AT). They tested the new parametrization by comparing it to a numerical cloud model and found a good agreement between the parametrization and the model. Later Kumar et al. (2011a) reported laboratory measurements of CCN activity and droplet activation kinetics of aerosols dry generated from clays, calcite, quartz, silica and desert soil samples. They used FHH adsorption activation theory for describing fresh dust CCN activity and found that the adsorption activation theory describes fresh dust CCN activity better than Köhler theory. Afterward, Kumar et al. (2011b) studied particle size distributions, CCN activity and droplet activation kinetics of wet generated aerosols from mineral particles and introduced a new framework of CCN activation of dust containing a soluble salt fraction, based on a combination of the traditional Köhler and FHH adsorption theories. Henning et al. (2010) on the other hand, studied agglomerated soot particles coated with levoglucosan and ammonium sulfate, and concluded that traditional Köhler theory was sufficient to describe the CCN activation of these mixed particles – as long as the amount of soluble material in the particles was known (see also Stratmann et al., 2010). Despite these pioneering studies, CCN activation measurements of partly insoluble particles containing a soluble fraction are still scarce.

Combustion processes result in emissions of different types of anthropogenic nanoparticles. Flame-made (fumed) silica (SiO_2) particles, mainly produced in flame reactors, are among these kind of particle types (Scheckman et al., 2009). Recently, fumed silica particles have been taken into consideration due to their industrial importance (Scheckman et al., 2009; Keskinen et al., 2011). In this study we use fumed silica particles as an experimental model to investigate the CCN activation of the insoluble and partly soluble particles and the applicability of the current theoretical frameworks developed to describe this phenomenon. Furthermore, since the presented theories generally assume that the insoluble particles are spherical, the agglomerated structure of the silica particles could cause uncertainties in the CCN activation parametrizations. Taking into account the shape characterization of aggregated silica particles may overcome these uncertainties. Different studies have recently focused on parametrizing the structure of aggregated particles, especially silica agglomerates (Fuchs, 1964; DeCarlo et al., 2004; Virtanen et al., 2004; Biskos et al., 2006; Scheckman et al., 2009).

The main aims of this study are (1) measuring the CCN activity of pure and mixed soluble–insoluble particles, (2) analysing and comparing the experimental results with theoretical calculations using the existing frameworks and (3) connecting the mass analysis and shape characterization of agglomerated silica particles to the existing theoretical frameworks to gain a better understanding of the structure effects of these particles. Laboratory measurements on the particle size distribution, mass, morphology and CCN activation of insoluble fumed silica mixed with different amounts of soluble materials have been conducted. Furthermore, the experimental CCN activity results are compared to theoretical calculations using the framework introduced by Kumar et al. (2011b), and the distribution of soluble material on wet-generated particle populations was discussed.

Table 1. Thermodynamic properties of components used in this study.

	Molar mass ($g\,mol^{-1}$)	Density ($g\,cm^{-3}$)	Solubility in water (mass %)	κ
$(NH_4)_2SO_4$	132.14[a]	1.77[a]	43.3[a]	0.61[e]
Sucrose	342.3[a]	1.58[a]	67.1[a]	0.084[f]
BSA	66 500[b]	1.362[b]	60[d]	0.013[g]
SiO_2	60.08[a]	2.16[c]	–	–

[a] Haynes et al. (2013). [b] Mikhailov et al. (2004). [c] Grayson (1985).
[d] Shiraiwa et al. (2011). [e] Petters and Kreidenweis (2007). [f] Ruehl et al. (2010).
[g] This work.

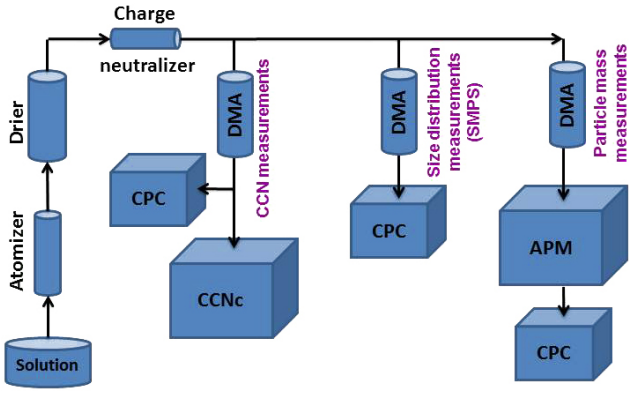

Figure 1. Schematic of the experimental setup and three types of measurements: CCN activity measurements, size distribution measurements by SMPS and particle mass analysing by APM.

2 Experimental setup

Pure soluble or insoluble and mixed soluble–insoluble particles were generated and analysed in this study. The investigated mixed particles consisted of fumed silica (Degussa, Aerosil-90) as the insoluble part and three different hygroscopic components as the soluble part. The first hygroscopic component was ammonium sulfate which is a water-soluble inorganic salt with high hygroscopicity (Table 1); the second one was sucrose which is a sugar, i.e. a water-soluble organic; the third one was bovine serum albumin (BSA) which is a large water-soluble protein with molecular dimensions of approximately $4 \times 4 \times 14$ nm (Sugio et al., 1999; Jeyachandran et al., 2010). The SiO_2 used in the experiments was hydrophilic fumed silica, with a specific surface area of $90\,m^2\,g^{-1}$ and purity of $\geq 99.8\,\%$ from Evonik Industries. Ammonium sulfate and BSA were purchased from Sigma-Aldrich, and sucrose was purchased from VWR International BVBA. All chemicals had purities higher than 99 %.

Figure 1 shows a schematic of the experimental setup used in this study. Pure silica and pure soluble particles as well as mixed particles made of silica and soluble species were produced using the atomization-drying method described in Keskinen et al. (2011). Particles were generated by an aerosol generator (Model 3076, TSI Inc., USA) after dissolving materials in deionized water (Model Maxima LS, USF Elga Ltd) with the production resistivity > 10 MΩ cm and total organic carbon concentration < 5 ppb. The solute content in the water suspension was 0.06 wt %. For mixed particles, the ratios of soluble components to silica were 1 : 19, 1 : 9 and 1 : 3, implying that the fractions of soluble species were expected to be 5, 10 and 25 % of total particulate mass in the atomized solution. We use the term solution, despite the fact that the insoluble silica particles were suspended in the water (instead of dissolved).

After the particles had been produced they were fed into a diffusion drier (Fig. 1) consisting of a porous tube surrounded by silica gel (Rotronic AG, model HC2-C04), resulting in a relative humidity (RH) below 5 % and they were neutralized using a charge neutralizer. Thereafter particle number size distributions were measured using a scanning mobility particle sizer (SMPS). The SMPS system was composed of an electrostatic classifier, which included a differential mobility analyser (DMA) (Model 3071; TSI, Inc.) to bin the particles according to electrical mobility, and an ultrafine condensation particle counter (CPC, model 3025; TSI, Inc.) to count the size-binned particles exiting the DMA.

Simultaneously, size-resolved CCN activity of the generated particles was measured using a CCN counter (CCNc; Droplet Measurement Technologies Inc.) (Roberts and Nenes, 2005) (Fig. 1). Before entering the CCNc, particles were size classified by a DMA, of the same model as the DMA used in the SMPS. The CCNc operates by supersaturating sample air to the point where the CCN become detectable particles. Humidified sheath air ($454\,cm^3\,min^{-1}$) surrounds the sample flow ($45.4\,cm^3\,min^{-1}$) in the CCN column to hold it in the centre of the column in the region of maximum supersaturation. The ratio of the flows was around 1 part of sample air to 10 parts of sheath air and the total flow rate was $500\,cm^3\,min^{-1}$. The supersaturation in the column could be varied between 0.1 and 1.5 %. The total number concentration of the particles entering the CCNc was measured by a CPC (Model 3772; TSI, Inc.) and the number of activated droplets was counted by an optical particle counter (OPC) over 20 size bins in the diameter range from 0.75 to 10 µm.

The effect of the silica particle morphology on activation was investigated by measuring the mass of size classified particles by aerosol particle mass analyser (APM) (model APM-3600; Kanomax Inc.) (Fig. 1) (McMurry et al., 2002; Park et al., 2003a and 2003b). The APM provides a direct relationship between the applied voltage, rotation speed, and particle mass (Liu et al., 2012). Therefore, by measuring the outlet number concentration of the APM corresponding to different applied voltages of the instrument, it was possible to measure the mass distribution of the size selected particles. For each APM voltage, the downstream number concentration was measured by a CPC (Model 3772; TSI, Inc.) (Fig. 1). From the voltage corresponding to the highest concentration the average particle mass was calculated using the following equation (McMurry et al., 2002; Park et al., 2003b):

$$m = \frac{qV}{r^2\omega^2 \ln(r_2/r_1)}, \quad (1)$$

where m is the particle mass, ω is the APM angular speed, V is the applied voltage, q is the particle charge, and r_1, r_2 and r are the inner, outer and rotating radius of the instrument, respectively.

3 Theoretical frameworks

3.1 Non-sphericity of particles

Particle shape can affect the physical dimensions of the particle in terms of the surface available for water vapour to adsorb onto, as well as for the effective curvature determining the Kelvin effect (see e.g. Kumar et al., 2011a). In the case of highly non-spherical or porous particles the conversion between the electrical mobility (the quantity measured with the SMPS system) and the available surface area or particle volume and density is not straightforward. As mentioned above, we used measurements of particle mass for the pure silica agglomerates to complement the information about the mobility of these particles.

Two parameters, the dynamic shape factor and fractal dimension, have been widely used to characterize non-sphericity of aerosol particles. Dynamic shape factor is defined as the ratio of the drag force on the agglomerated particles to the drag force on the volume equivalent spherical particles (χ', volume-based shape factor) or to the drag force on the mass equivalent spherical particles (χ, mass-based shape factor) (Kelly and McMurry, 1992; DeCarlo et al., 2004). The fractal dimension (D_f) is the coordination number in the aggregate and links properties like surface area of a particle to the scale of the measurements (Hinds, 1999; Ibaseta and Biscans, 2010). These parameters are applicable to quantify the morphology of agglomerated particles.

The mass-based shape factor is defined as (Kelly and McMurry, 1992)

$$\chi = \frac{d_b}{d_{me}} \cdot \frac{C(d_{me})}{C(d_b)}, \quad (2)$$

where d_b and d_{me} are mobility diameter and mass equivalent diameter, while $C(d_b)$ and $C(d_{me})$ are the corresponding Cunningham slip correction factors. The slip correction factors are given by (Kulkarni, et al., 2011)

$$C(d_i) = 1 + \frac{2\lambda}{d_i}\left(1.142 + 0.558\exp\left(-0.999\frac{d_i}{2\lambda}\right)\right), \quad (3)$$

where λ is the mean free path of the gas molecules and d_i corresponds to either of d_{me} or d_b. The mass equivalent diameter (d_{me}) was calculated using the following equation (Kelly and McMurry, 1992):

$$d_{me} = \left(\frac{6\,m}{\pi\,\rho_p}\right)^{1/3}, \quad (4)$$

where ρ_p is the material density of the silica particle (see Table 1).

To calculate the volume and surface equivalent diameters (d_{ve} and d_{se}) of the silica particles, which will be required to estimate the CCN capability of these particles, in addition to the mobility and mass data, knowledge on the volume-based shape factor (χ') is also required (see DeCarlo et al., 2004 and Kumar et al., 2011a, for details):

$$\frac{d_{ve}}{C(d_{ve})} = \frac{d_b}{\chi \cdot C(d_b)} \quad (5)$$

$$d_{se} = \frac{3\chi d_{ve} - d_b}{2}. \quad (6)$$

In this regard two limiting assumptions can be made. The first one is to assume compact agglomerates with nearly spherical shape and internal voids. In this case the mobility and volume equivalent diameters are approximately equal ($\chi' = 1$) and also equal to the surface equivalent diameter, but larger than the mass equivalent diameter, i.e. $d_b = d_{ve} = d_{se} > d_{me}$. The particle density is in this case lower than the pure silica material density, but equal to the effective density. The second assumption is to approximate the silica particles as chain-like agglomerates with no internal voids, for which mass and volume equivalent diameters are equal ($\chi = \chi'$), but smaller than surface equivalent and mobility diameters, i.e. $d_{ve} = d_{me} < d_{se}$ and d_b. In this case the particle density would be the same as the pure silica material density but higher than the effective density.

The fractal dimension (D_f) of the silica particles provides further insight on their sphericity (DeCarlo et al., 2004; Boldridge, 2010; Keskinen et al., 2011): for perfect spheres $D_f = 3$ and for line-like structures $D_f = 1$.

The fractal dimension of the pure silica particles was determined using the scaling law for effective density versus mobility diameter (Skillas et al., 1998, 1999):

$$\rho_e \propto d_b^{(D_f - 3)}, \quad (7)$$

where ρ_e is the particle effective density. The ρ_e was estimated using the following equation (Virtanen et al., 2004):

$$\rho_e = m / \left(\pi d_b^3/6\right), \quad (8)$$

where m is the mass of the particles determined using APM (Eq. 1).

3.2 CCN activation of soluble particles

κ-Köhler theory (Petters and Kreidenweis, 2007) was used to estimate the critical supersaturation of pure ammonium sulfate, sucrose and BSA particles. The saturation ratio (S) is expressed as

$$S = \frac{d_p^3 - d_{dry}^3}{d_p^3 - d_{dry}^3(1-\kappa)} \exp\left(\frac{4\sigma_w M_w}{RT\rho_w d_p}\right), \quad (9)$$

where σ_w is the water surface tension, ρ_w is the water density, M_w is the molar mass of water, R is the universal gas constant, T is the temperature, d_{dry} is the dry particle diameter, d_p is the droplet diameter and κ is the hygroscopicity parameter of soluble particles.

The supersaturation (s) is equal to ($S-1$) and is expressed as a percentage. The maximum value of the supersaturation is called critical supersaturation (s_c) – similar definition naturally holding for critical saturation ratio S_c as well. Thus, at the critical point,

$$\left.\frac{ds}{dd_p}\right|_{d_p=d_c} = 0, \quad (10)$$

where d_c is called the critical diameter. The κ values for pure soluble particles were extracted from previous studies or, in the case of BSA, derived by applying the following relation introduced by Petters and Kreidenweis (2007) to our observations of the critical supersaturations of the pure soluble particles:

$$\kappa = \frac{4A^3}{27 d_{dry} \ln^2 S_c}, \quad (11)$$

where S_c is the saturation ratio at the critical point, $A = \frac{4\sigma M_w}{RT\rho_w}$, $\sigma = 0.072\,\mathrm{J\,m^{-2}}$, $T = 298.15\,\mathrm{K}$, $M_w = 0.018\,\mathrm{kg\,mol^{-1}}$ and $\rho_w = 1000\,\mathrm{kg\,m^{-3}}$.

The pure soluble particles were assumed to be compact and spherical, and thus the mobility diameter was used as the d_{dry} in Eqs. (9)–(11).

3.3 CCN activation of insoluble silica

The critical supersaturation of pure silica particles was calculated using FHH adsorption theory (Sorjamaa and Laaksonen, 2007, Kumar et al., 2009, 2011a). In this case the relationship between water supersaturation s and particle size can be expressed as

$$s = \frac{4\sigma_w M_w}{RT\rho_w d_p} - A_{FHH}\left(\frac{d_p - d_{dry}}{2d_{H_2O}}\right)^{-B_{FHH}}, \quad (12)$$

where $d_{H_2O}(= 2.75\,\text{Å})$ is the diameter of the water molecule, and A_{FHH} and B_{FHH} are the FHH adsorption isotherm parameters. The first and second terms on the right-hand side of Eq. (12) correspond to the contributions from the Kelvin and adsorption effects, respectively.

In the literature, different values of the parameters A_{FHH} and B_{FHH} for silica particles have been reported. Kumar et al. (2011a) obtained the values 2.95 and 1.36 for A_{FHH} and B_{FHH} of quartz silica, respectively, and Keskinen et al. (2011) assigned values of 4.82 and 2.16 for A and B for non-agglomerated fumed silica particles (Degussa, Aerosil-300) with the diameter of 8 and 10 nm.

To yield a reasonable estimate of the surface available for adsorption, the surface equivalent diameter of the pure silica particles was used as d_{dry} in Eq. (12).

3.4 CCN activation of mixed soluble and insoluble particles

Kumar et al. (2011b) used adsorption activation theory assuming that the particles are spheres and presented a model describing mixed particles with an insoluble and a soluble fraction. They introduced the following relation between water supersaturation, particle size and composition:

$$s = \frac{4\sigma_w M_w}{RT\rho_w d_p} - \frac{\varepsilon_s d_{dry}^3 \kappa}{\left(d_p^3 - \varepsilon_i d_{dry}^3\right)} - A_{FHH}\left(\frac{d_p - \varepsilon_i^{1/3} d_{dry}}{2d_{H_2O}}\right)^{-B_{FHH}}, \quad (13)$$

where ε_i and $\varepsilon_s = 1 - \varepsilon_i$ are the insoluble and soluble volume fractions in the dry particles and κ is the hygroscopicity parameter of the soluble part. A_{FHH} and B_{FHH} are the FHH adsorption isotherm parameters of the insoluble part, which is assumed to interact with the water through adsorption onto its surface.

To estimate the average insoluble volume fractions of the mixed particles, the following relation was used:

$$\varepsilon_i = \frac{m_i/\rho_i}{m_i/\rho_i + m_s/\rho_s}, \quad (14)$$

where m_i and m_s are the insoluble and soluble mass fractions in the total mixed aerosol population, and ρ_i and ρ_s are the densities of the insoluble and soluble parts, respectively. The bulk densities of the used components are listed in Table 1.

In the second term of Eq. (13) the volume equivalent diameter was used as d_{dry}, while the surface equivalent diameter was assumed to represent the d_{dry} in the last term.

4 Results and discussion

4.1 Particle size distributions

The SMPS measurements yielded the average number size distributions for silica particles mixed with $(NH_4)_2SO_4$, sucrose and BSA (Fig. 2). Figure 2a displays average number size distributions for particles made of pure fumed silica, pure $(NH_4)_2SO_4$ and particles made of silica and different amounts of $(NH_4)_2SO_4$. As is evident in the figure, size distributions of particles generated from pure silica or pure $(NH_4)_2SO_4$ are unimodal while size distributions of particles generated from the silica–$(NH_4)_2SO_4$ mixtures are bimodal. The mean mobility diameter is ~ 30 nm for the pure $(NH_4)_2SO_4$ particles, and approximately 150 nm for the pure silica particles. The first mode of the bimodal size distributions, associated with particles generated from the aqueous bulk mixtures, is centred at a diameter of less than 30 nm. The second mode, with lower number concentration, is centred at approximately 150 nm. Figure 2b shows the average number size distributions of particles made of sucrose and silica. Particles made of pure sucrose have a mean diameter of approximately 50 nm. Size distributions associated with particles generated from the silica–sucrose mixtures are bimodal (Fig. 2b); the first mode centred at a diameter of less than

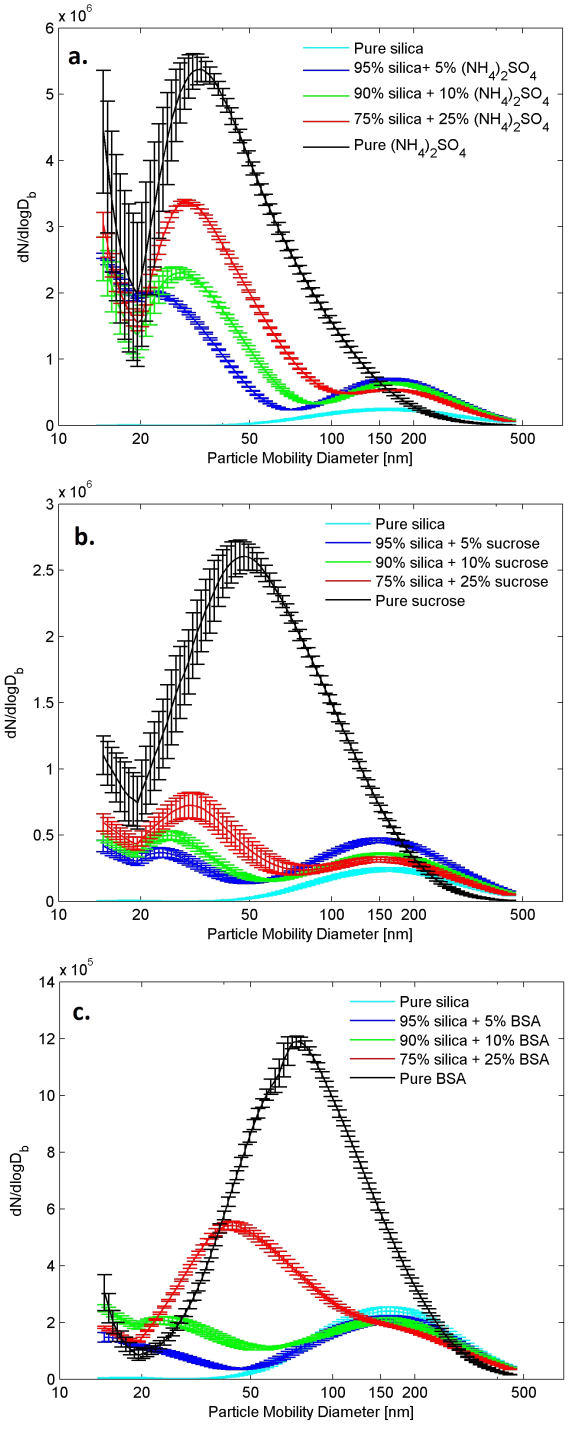

Figure 2. Average particle number size distributions (SMPS) for silica particles mixed with **(a)** $(NH_4)_2SO_4$, **(b)** sucrose and **(c)** BSA. Each average size distribution is based on at least 70 individual size distributions, and the error bars represent the standard deviation of the measurements.

50 nm and the second mode centred at a diameter of about 150 nm. Similarly, Fig. 2c shows the average SMPS number size distributions of particles made of silica and BSA. These data are comparable with previous two measurements in Figs. 2a–b. The particles made of the large BSA protein have a mean diameter of about 75 nm. The mode associated with particles made of a mixture of BSA and silica is centred at about 150 nm.

In the case of mixed aerosols, the particles in the first mode of the bimodal size distributions are likely pure soluble particles, while the second mode of the bimodal distribution curves represents silica particles mixed with soluble species. Hence, when analysing the activation behaviour of mixed particles we omitted the CCNc data of the smallest particles by subtracting their contribution from the CCN numbers and restricted our analysis to particle sizes larger than 100 nm.

To estimate the average soluble volume (mass) fractions in the mixed particles, we calculated the fraction of soluble material lost to the first pure mode of the particle size distributions and subtracted it from the total soluble mass. In this regard, we fitted log-normal distribution curves to the number size distributions associated with particles from the mixtures and estimated the volume and mass distributions related to each particle number size distribution. Hereupon, it was possible to estimate the fraction of total soluble mass remaining in the first mode of the bimodal size distributions for each mixture, and the fraction of the total soluble mass which was mixed with silica (Table 2). By multiplying this fraction with the soluble mass fraction in the bulk mixture we gained an estimate of the real average soluble mass fraction in the mixed/coated particles excluding the portion of the pure soluble particles. As is evident from Table 2, the overall mass losses of the soluble material from the first mode are small, and 87–100 % of the total soluble masses were mixed with silica particles.

4.2 Mass analysis and size characterization of pure and mixed silica particles

Since fumed silica particles are agglomerates, mass analysis of the pure silica particles could help us to get a better understanding of their shape (see Sect. 3.1). As an example, Fig. 3a shows the observed average number concentrations of 100 nm size-selected silica particles (by DMA) for different APM voltages. A log-normal distribution was fitted to provide the voltage value corresponding to the peak of the distribution. After determining the mass of size selected particles using Eq. (1), the effective density of the silica particles was estimated (Eq. 3). The APM measurements were performed for two different rotation speeds of the APM (3000 and 5000 rpm). The achieved effective particle densities using these two rotation speeds are presented in Fig. 3b. There is only a small difference in effective density between the two different speeds, giving confidence in the results. Fig-

Table 2. The total soluble fraction of the solute masses in the bulk mixtures, the fraction of total soluble mass mixed with silica, the average soluble mass fraction of the mixed particles (calculated from particle size distributions, see text for details).

Soluble mass fraction in the bulk mixture (%)	Fraction of total soluble mass mixed with silica (%)			Total soluble mass fraction in the mixed particles (%)		
	Silica + $(NH_4)_2SO_4$	Silica + sucrose	Silica + BSA	Silica + $(NH_4)_2SO_4$	Silica + sucrose	Silica + BSA
25	92	98	87	23.4	24.6	22.5
10	88	99	99	8.9	9.9	9.9
5	87	99	~ 100	4.4	4.9	~ 5

ure 3c displays the mass-based shape factor (χ) of silica particles for different mobility diameters. The χ is clearly larger than 1 and increases by increasing mobility diameter. This indicates that internal voids and/or irregularities of the particles increase with increasing particle diameter (Kelly and McMurry, 1992).

The fractal dimension of the silica particles was estimated using the slopes of the curves in Fig. 3b and Eq. (6) yielding D_f values of 2.54 and 2.55 for the 3000 and 5000 rpm rotation speeds, thus suggesting closer to spherical rather than rod- or chain-like structures. The fitted D_f values are also close to the value ($D_f = 2.57$) reported by Keskinen et al. (2011) and Ibaseta and Biscans (2010) ($D_f = 2$ to 2.5) for fumed silica (Degussa, Aerosil-300 and -200, respectively). We therefore expect the silica particles to be better represented by the "compact agglomerates" assumption and applying this assumption ($\chi' = 1$, see Sect. 3.1), the volume and surface equivalent diameters used in all the CCN activity calculations were thus approximated with the mobility diameters.

The mass analysis results were only available for the pure silica particles. When analysing the CCN activation data for the mixed particles, we assumed that the effective density of the silica in the mixed particles was similar to the effective density of the pure silica particles. The physical meaning of this assumption would be that the silica present in the mixed particles would contain the same volume of voids per unit silica mass as the pure particles. Furthermore, when calculating the critical supersaturations using Eq. (13) the adsorption term was calculated using the surface equivalent diameter d_{se} as d_{dry} and the solubility term using the volume equivalent diameter d_{ve} as d_{dry}, which in our case, by compact agglomerates assumption $d_{ve} = d_{se} = d_b$.

4.3 CCN activation results

Before analysing the CCN activity of the generated particles, all the activation curves were charge-corrected using the procedure introduced by Moore et al. (2010). The ratio of the corrected CCN and CN (condensation nuclei, measured by CPC) time series thus determines the activated fraction (also referred to as activation ratio) of the specified particles (Kumar et al., 2011a). Furthermore, as described in Sect. 4.3.2, for the mixed particles the contributions of the smaller completely soluble particle mode (see Fig. 2) were subtracted from the CCN concentrations. Finally, all the activation curves used in the further analysis were normalized using a correction factor derived from the ammonium sulfate (AS) experiments, assuming that AS activation probability reaches unity at high supersaturations. In the cases where the normalization with the AS data would have produced CCN / CN values larger than unity, the value was set to unity instead.

4.3.1 CCN behaviour of pure components

Figure 4 shows the activation ratio dependence on supersaturation for 120 nm (mobility diameter) pure silica, BSA, sucrose and ammonium sulfate particles. A sigmoid curve was fitted to each set of activation ratio data. Critical supersaturation (s_c) is often associated with the supersaturation where 50 % of the particles are CCN activated – equivalent to a CCN / CN ratio of 50 %, and we will follow this convention although the two are not necessarily equal when the CCN / CN curve is not a step function. As expected, $(NH_4)_2SO_4$ particles, which are the most hygroscopic particles investigated in this study (see κ values in Table 1), activated at lower supersaturations than was the case for sucrose, silica and BSA particles. The pure silica particles, which are insoluble and non-hygroscopic, exhibited the highest critical supersaturation of the investigated compounds (Fig. 4).

Figure 5 displays activation ratio against supersaturation for pure silica particles of different mobility diameters. As is evident from Fig. 5, the critical supersaturation decreases with increasing particle diameter. Experimentally and theoretically determined critical supersaturations of pure silica particles as a function of particle mobility diameter are shown in Fig. 6. Previously, the values for FHH adsorption parameters (Eqs. 10 and 12) of different types of silica have been determined by Kumar et al. (2011a) (quartz), and Keskinen et al. (2011) (fumed silica, Aerosil-300). To compare our results to these studies, we fitted the FHH adsorption parameters for the pure silica particles (fumed silica, Aerosil-90). A_{FHH} and B_{FHH} values of 2.50 and 1.62 explain our results on the activation diameter vs. critical supersaturation (Fig. 6), although the fits were difficult to constrain uniquely. Our results are closer to those reported by Keskinen et al. (2011) than Kumar et al. (2011a), but the A_{FHH} and B_{FHH} values are close to those reported by Kumar et al. (2011a). This highlights the sensitivity of the fits to adsorption parameters,

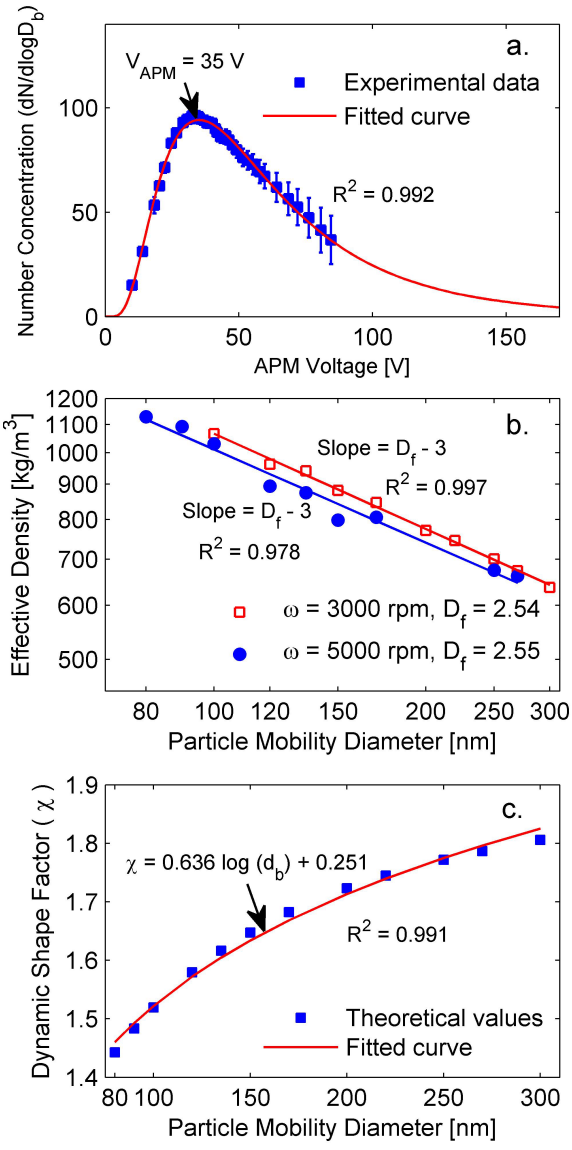

Figure 3. (a) Average number concentration of 100 nm (mobility size) pure silica particles downstream the APM and at a rotation speed of the APM of 3000 rpm. The number concentrations were averaged over 1 min for each APM voltage, and the error bars represent the standard deviation of about 60 measurements recorded under the same conditions. **(b)** Effective density of silica particles for different mobility diameters and two different rotation speeds of the APM (3000 and 5000 rpm). The fitted fractal dimensions are 2.54 and 2.55, respectively. **(c)** Mass-based shape factor versus electrical mobility diameter for silica particles.

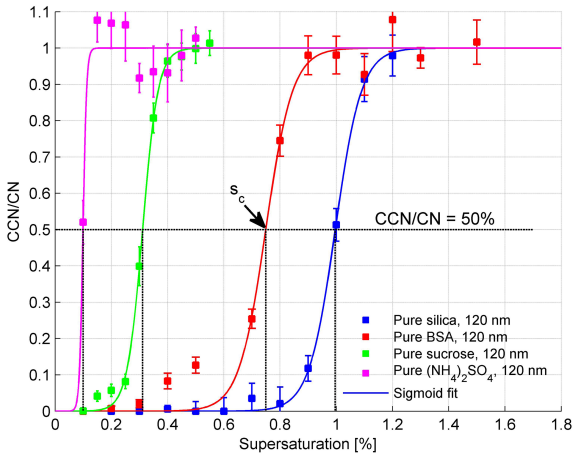

Figure 4. The average activation ratio of pure soluble or insoluble particles with the mobility diameter of 120 nm at different supersaturations. Error bars represent the standard deviation of the activation efficiency of about 20 measurements corresponding to each supersaturation of the instrument. Critical supersaturation s_c is defined as the point where the activation ratio is equal to 50 %.

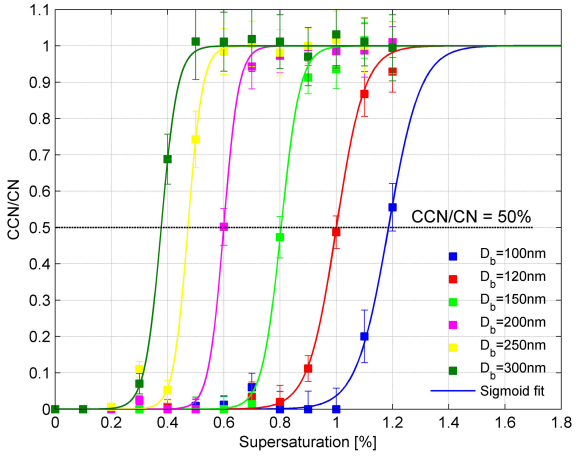

Figure 5. The average activation ratio versus supersaturation for different mobility diameters of silica particles. Error bars represent the standard deviation of the measured activation efficiency as a result of about 20 measurements corresponding to each supersaturation of the instrument.

reflecting the fact that our data set is not sufficient for constraining any physical or chemical phenomena behind these values. In particular, the parameter A_{FHH}, describing the interactions of the first monolayer with the adsorbent surface, seems to be difficult to constrain based on the CCN activation data. This is perhaps not surprising as at the point of activation the rapid condensation of water might relatively soon destroy the information of the very first steps of the adsorption/monolayer formation. For the parameter B_{FHH}, on the other hand, the fits seem to reproduce relatively robust values. CCN activation measurements are probably not the best approach for yielding accurate data of the physical phenomena behind the adsorption parameters – as a lot of information has already been lost at the point where the CCN are activated and detected – but should be rather regarded as a valuable source of information on the processes limiting atmospheric cloud droplet formation. It should also be pointed out that the quartz silica (Kumar et al., 2011a) is not as hy-

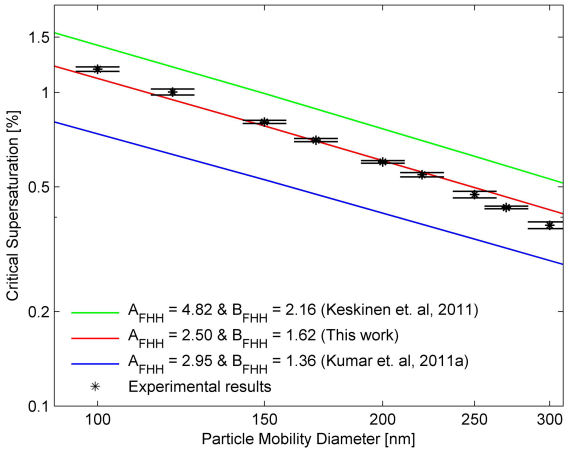

Figure 6. Critical supersaturations against activation mobility diameter of pure silica particles with different FHH adsorption isotherm parameters from different studies compared to experimental results. Error bars represent the minimum vs. maximum values of supersaturation to estimate the s_c corresponding to each d_b.

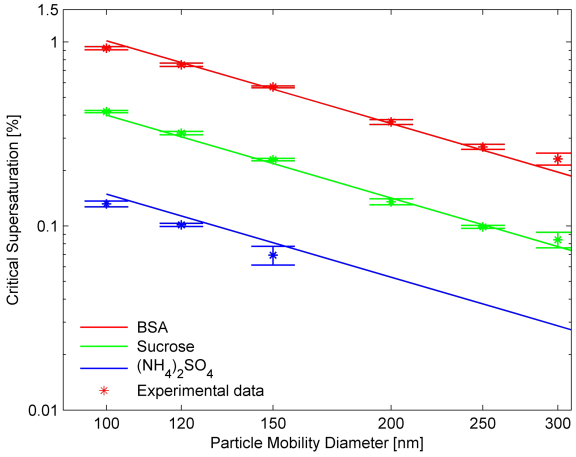

Figure 7. Experimental and theoretical critical supersaturations of pure $(NH_4)_2SO_4$, sucrose and BSA particles for different mobility diameters based on κ-Köhler theory. Error bars represent the minimum vs. maximum values of supersaturation to estimate the s_c corresponding to each d_b.

drophilic as fumed silica which probably affects the critical supersaturation. Furthermore, the FHH adsorption parameters in the Keskinen et al. (2011) study were fitted for only 8 and 10 nm fumed silica particles which were most likely spherical and thus potentially not fully representative of the agglomerated particles that we used. Impurity of the silica could also affect the results even though the deionized water was used in all studies. To conclude, the experimental results for s_c of pure silica particles were in good agreement with theoretical calculations using FHH adsorption isotherm and small deviations were only observed for larger diameters.

To estimate the critical supersaturations of pure soluble particles, κ-Köhler theory (Eqs. 9 and 10) was applied. Table 1 lists κ values of the soluble materials used in this study. The ability for ammonium sulfate particles to act as CCN has been widely studied (e.g. Garland, 1969; Kreidenweis et al., 2005; Hiranuma et al., 2011), and here we employed the previously reported hygroscopicity (κ) values (Petters and Kreidenweis, 2007), given the relatively good agreement between the κ value fitted to our results (0.78) and the literature values. The κ value for pure sucrose was extracted from (Ruehl et al. (2010), which was also in reasonable agreement with the value 0.08 that best described our results. For the pure BSA particles κ was calculated based on Eq. (11) using the CCN activation results of pure BSA particles in this study. The experimentally and theoretically determined critical supersaturations for pure $(NH_4)_2SO_4$, BSA and sucrose particles are shown in Fig. 7. Indeed, κ-Köhler theory results using the literature values for the hygroscopicity parameter were in good agreement with the experimentally determined critical supersaturations of pure soluble particles.

4.3.2 CCN behaviour of the mixtures

Here we present the CCN activation results of co-synthesized silica particles mixed with $(NH_4)_2SO_4$, sucrose or BSA considering the determined total soluble fractions in the mixed particle population from Table 2.

The activation ratio curves were determined for different diameters of mixed particles and different ratios of soluble to insoluble materials. For mixed particles the activation ratio curves were modified by subtracting the contributions of the smaller completely soluble particle from the CCN and CN concentrations using the following procedure: first, the contribution of pure soluble particles to the total number of CN for each size were estimated by fitting two log-normal modes to the size distributions such as those shown in Fig. 2. The pure soluble mode was then subtracted from the CN data for each size to yield an estimate of the total numbers of mixed CN. Second, using the CCN / CN ratios of the pure soluble particles (shown for 120 nm in Fig. 4) we could estimate the number of CCN originating from pure CN at each mobility diameter and supersaturation. Subtracting this from the total number of CCN, we could yield an estimate for the CCN / CN ratio for the mixed particles. Figure 8 represents the activation ratio curves for 150 nm (mobility diameter) pure and mixed particles. Although both the raw data (unnormalized) and the normalized curves are shown for completeness, only the normalized data were used in the follow-up analysis. It can be seen that the normalization procedure caused only very small adjustments to the 50 % points inferred from the curves.

Figure 8a shows the activation probabilities of mixed silica–$(NH_4)_2SO_4$ particles. The critical supersaturation (corresponding to CCN / CN = 50 %) is higher for pure sil-

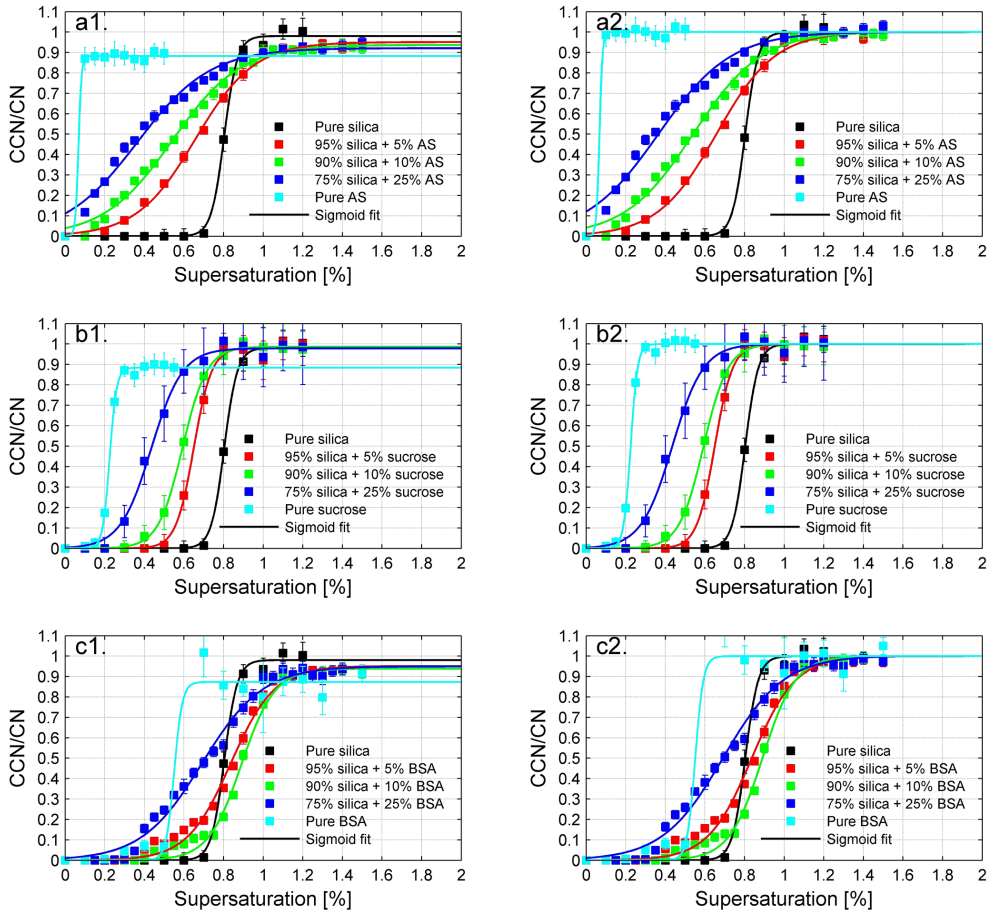

Figure 8. (a) Activation ratio curves for different supersaturations of silica + $(NH_4)_2SO_4$ particles of 150 nm mobility diameter, **(b)** activation ratio curves for different supersaturations of silica + sucrose particles of 150 nm mobility diameter, **(c)** activation ratio curves for different supersaturations of silica + BSA particles of 150 nm mobility diameter. The activation curves on the left side (subplots a1–c1) represent the unnormalized data, while the activation curves on the right side (subplots a2–c2) show the normalized ones. Error bars represent the standard deviation of the measured activation efficiency as a result of about 20 measurements corresponding to each supersaturation of the instrument.

ica particles than for the particles with soluble material. Evidently, the pure $(NH_4)_2SO_4$ particles have the lowest critical supersaturation. Furthermore, the critical supersaturation decreases when the fraction of soluble material in the particles increases, and the CCN / CN curves are shallower (i.e. further from a step function) for the mixed as compared with the pure particles. The same behaviour can be observed in Fig. 8b for 150 nm silica particles mixed with sucrose. Pure sucrose particles were activated at a supersaturation of 0.22 % which is comparable to previous studies (e.g. Rosenorn et al., 2006). The s_c decreases with increasing sucrose ratio in the mixed particles, similar to what was observed for ammonium sulfate in Fig. 8a. In the case of particles containing BSA, however, a different behaviour was observed: s_c was higher for particles made of 5 and 10 % BSA than for particles made of pure silica (Fig. 8c). The reason for this behaviour is not clear but it is known that adsorption of BSA on silica can affect the structural properties of BSA. As was explained by Larsericsdotter et al. (2005), for soft proteins such as BSA the structural stability decreases when adsorption onto other materials occurs. On the other hand, the BSA can also affect the agglomerate structure of the mixed particles – for instance through more compact agglomerates with increasing BSA concentrations (see e.g. Kiselev et al., 2010 and Stratmann et al., 2010 for discussion on effects of coating on agglomerate compactness). However, it is also possible that this effect is solely due to different distribution of the soluble materials as a function of particle size for the different bulk solution compositions, which is discussed in detail below.

To estimate the soluble mass fractions (ω_s) in the coated/mixed particles required for the application of Eq. (13), the total amount of soluble material was first estimated by fitting log-normal size distributions to the observed size distributions (Sect. 4.1). The dashed lines in Fig. 9 show the theoretical critical supersaturations (using Eq. 13) of par-

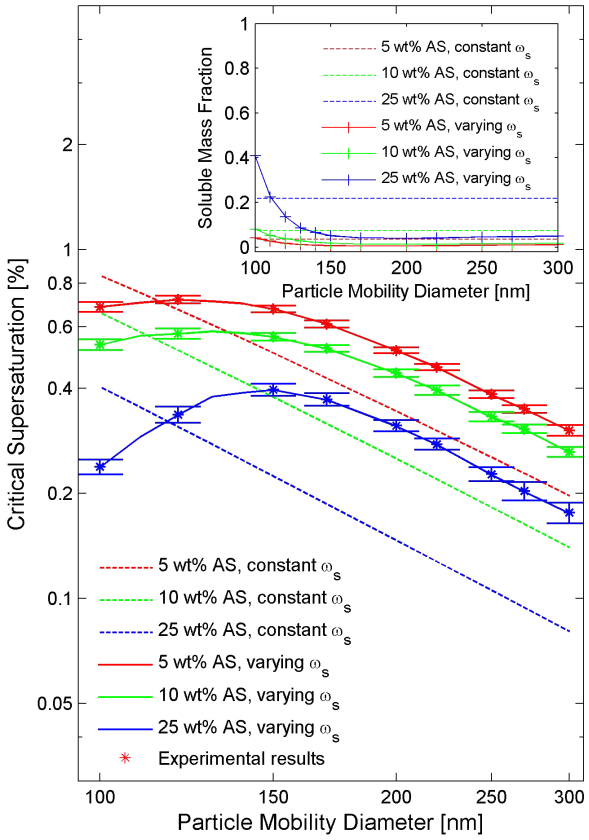

Figure 9. Experimental and theoretical critical supersaturations for mixed silica + $(NH_4)_2SO_4$ (AS) particles for different particle mobility diameters using the model of Kumar et al. (2011b). Dashed lines represent calculated critical supersaturations based on an assumption of constant soluble mass fractions (ω_s) with changing diameter and solid lines show the critical supersaturations based on the size-dependent soluble mass fractions. Error bars represent the minimum vs. maximum values of supersaturation to estimate the s_c corresponding to each mobility diameter. The inset represents assumed constant soluble mass fractions as well as size-dependent ones corresponding to the 50 % points in the CCN / CN curves for different size vs. supersaturation pairs of mixed silica + $(NH_4)_2SO_4$ particles.

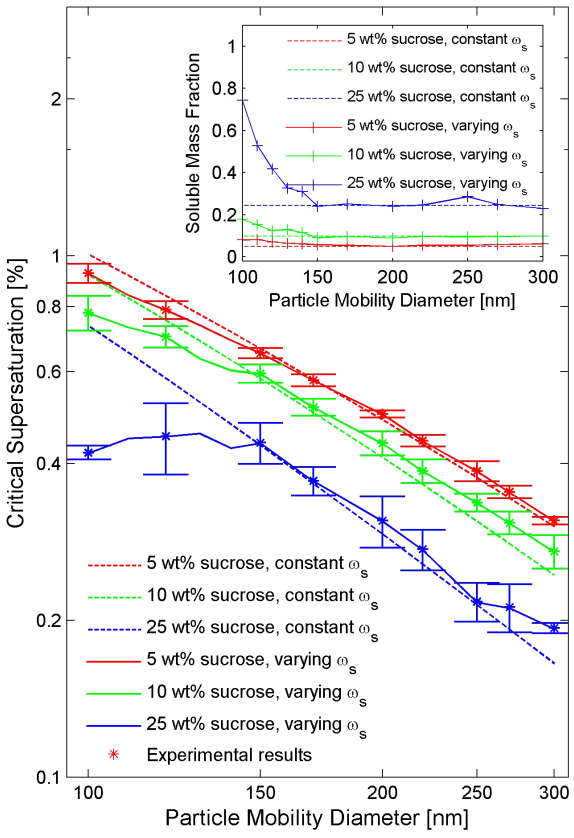

Figure 10. Experimental and theoretical critical supersaturations for mixed silica + sucrose particles for different particle mobility diameters using the model of Kumar et al. (2011b). Dashed lines represent calculated critical supersaturations based on an assumption of constant soluble mass fractions (ω_s) with changing diameter and solid lines show the critical supersaturations based on the size-dependent soluble mass fractions. Error bars represent the minimum vs. maximum values of supersaturation to estimate the s_c corresponding to each mobility diameter. The inset represents assumed constant soluble mass fractions as well as size-dependent ones corresponding to the 50 % points in the CCN / CN curves for different size vs. supersaturation pairs of mixed silica + sucrose particles.

ticles consisting of a mixture of silica and ammonium sulfate assuming soluble volume fractions (ε_s) corresponding to these constant ω_s (see Table 2 and the dashed lines of the inset in Fig. 9) with changing diameter. These theoretical values of critical supersaturations are mostly lower than the observed critical supersaturations (stars), and the size-dependence of the critical supersaturation is not captured by the theory. We observed the same (although less pronounced) behaviour for silica particles mixed with sucrose and BSA (Figs. 10 and 11). In all three cases, the observed critical supersaturations were higher than expected from the model by Kumar et al. (2011b) using constant soluble mass fractions. The calculations are very sensitive to the κ values and the deviation between experimental and estimated s_c for mixed particles increases with increasing hygroscopicity. The largest deviations were observed for particles mixed with $(NH_4)_2SO_4$, which is more hygroscopic ($\kappa = 0.61$) than the other compounds. The adsorption term contribution to the critical supersaturation in Eq. (13) was generally minor: < 0.72 % for silica + $(NH_4)_2SO_4$, < 3.8 % for silica + sucrose and < 7 % for silica + BSA of the total (Kelvin + solubility + adsorption) contribution for all the studied compositions and supersaturations. The theoretical predictions were thus dominated by the Kelvin and solubility effects – similarly to the case of soot agglomerates studied by Henning et al. (2010).

The small contribution of the adsorption term to the theoretical predictions combined with the shallow activation ratio curves (see Fig. 8) suggest that the reason for the apparent

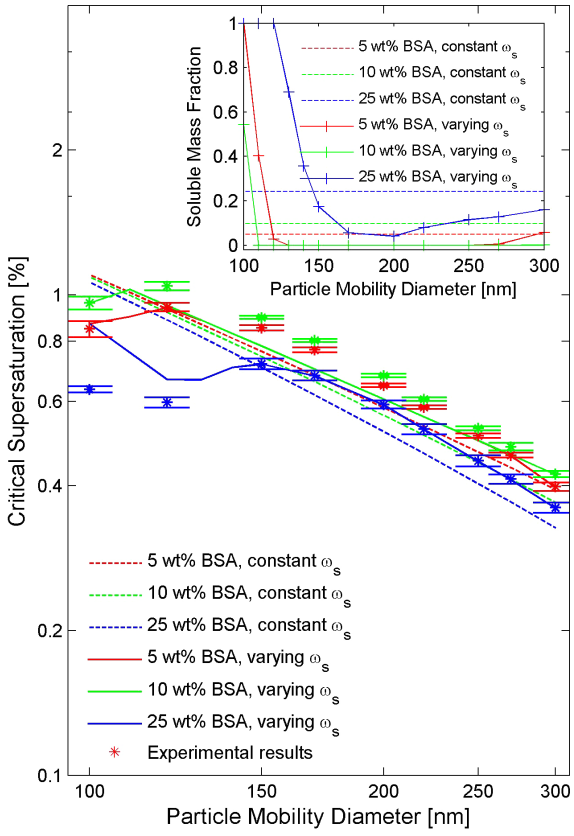

Figure 11. Experimental and theoretical critical supersaturations for mixed silica + BSA particles for different particle mobility diameters using the model of Kumar et al. (2011b). Dashed lines represent calculated critical supersaturations based on an assumption of constant soluble mass fractions (ω_s) with changing diameter and solid lines show the critical supersaturations based on the size-dependent soluble mass fractions. Error bars represent the minimum vs. maximum values of supersaturation to estimate the s_c corresponding to each mobility diameter. The inset represents assumed constant soluble mass fractions as well as size-dependent ones corresponding to the 50 % points in the CCN / CN curves for different size vs. supersaturation pairs of mixed silica + BSA particles.

discrepancy between the theoretical and the observed critical supersaturations is a non-constant distribution of the soluble material with varying particle size. This explanation seems particularly feasible taking into account the good agreement between the experiments and theory for the pure particles, and the fact that the particle generation method (atomization and drying of aqueous solutions) does not allow for controlling the ratio of soluble to insoluble materials at a given particle size – only for the overall aerosol population. To yield further insight into this, we estimated the distribution of the soluble material by fitting size-dependent ε_s distributions to the CCN / CN vs. s_c curves (e.g. Fig. 8) using Eq. (13) – thus assuming that all the mixed particles that activate at a given supersaturation interval contain a specific soluble volume (mass) fraction. It is worthwhile to note that the ε_s determined in this way corresponds to the surface or volume equivalent diameters (linked to the particle mass through the modified silica density including internal voids, see Sect. 3), and is thus not directly comparable to the mass fractions in the atomized solution.

The s_c (defined as the 50 % point in the CCN / CN curves) vs. mobility diameter results obtained through the fitting procedure are shown by the solid lines in Figs. 9–11, and the resulting soluble mass fractions ω_s corresponding to the ε_s fitted to the 50 % points in the CCN / CN curves as a function of particle size are shown as the solid lines in the insets. The results suggest a very uneven distribution of the soluble material as a function of particle size: the small particles contain considerably higher fractions of soluble material than the larger ones, and the effect increases with the amount of soluble material. In the case of BSA (Fig. 11), the different mixture compositions lie relatively close to each other in terms of their critical supersaturations – making it difficult to constrain the soluble contents of these particles. However, it seems clear that at the small particle sizes (< 150 nm) the particle population is dominated by pure BSA particles. At sizes between 150 and 250 nm, on the other hand, extremely low BSA content is required to reproduce the observed critical supersaturations. This is of course also visible in Fig. 8c, where the mixtures with low BSA content seem to activate at even higher supersaturations than pure silica. The exact reason for this is not clear, but the effect of BSA on silica particle structure (e.g. density, etc.) could be speculated upon.

While the size-dependent ω_s shown in Figs. 9–11 corresponds to the points at which 50 % of the CN activate as CCN for a given particle diameter and supersaturation, the ω_s values vary even for a given particle size – as indicated by non-step function shape of the activation curves in Fig. 8. An example distribution of the soluble mass as deduced from the CCN / CN vs. s_c data (Fig. 8) using Eq. (13) is shown in Fig. 12 for the 150 nm mobility diameter mixed particles. The figure shows that for each mixture, there is an uneven distribution of soluble mass fraction in the particles of a given size. In all cases, there is a large number of particles with very low soluble mass fractions (less than initial bulk solution) and the composition of the size-selected particles is not constant. Similar conclusions were drawn by Dusek et al. (2006) for soot particles coated by NaCl. When compared to the mass fractions in the atomized solution, it can be seen that only in the case of sucrose are the distribution peaks at soluble mass fractions similar to the original solution, while the mixtures containing ammonium sulfate and BSA have widely varying compositions.

5 Summary and conclusions

In this study, the CCN activation of pure and mixed particles of silica and soluble compounds (AS, sucrose and BSA) was investigated. Furthermore, the morphology and effective

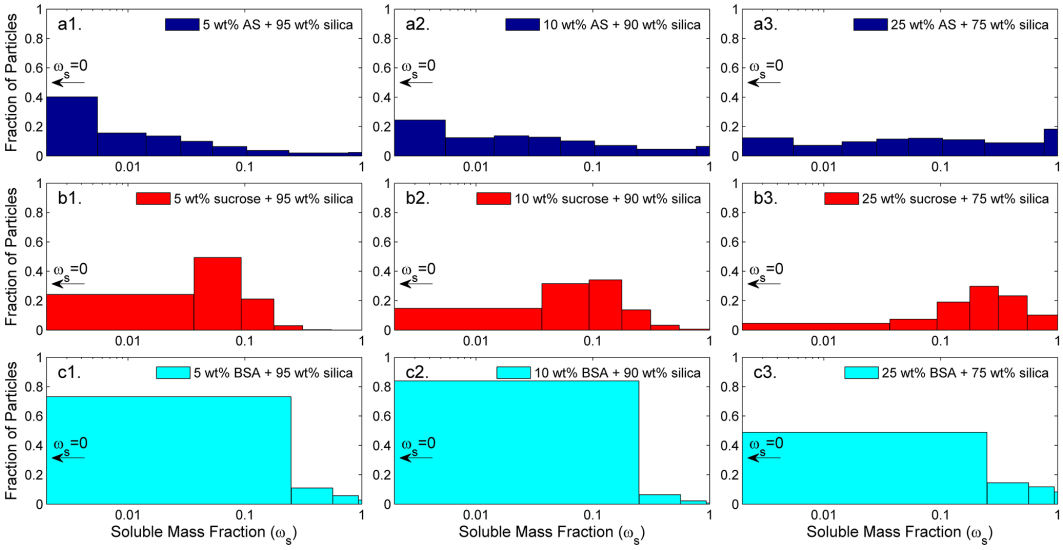

Figure 12. The distribution of soluble material on 150 nm (mobility diameter) particles in the mixed particles made of **(a1–a3)** silica + $(NH_4)_2SO_4$ (AS), **(b1–b3)** silica + sucrose, **(c1–c3)** silica + BSA. Note that the smallest solubility bin extends down to zero, i.e. particles consisting of pure silica.

density of silica particles were investigated based on APM measurements. In addition, size distributions of the sampled particles were measured using a SMPS. Then non-sphericity of the particles was investigated by applying APM measurements and estimating mass-based dynamic shape factors and fractal dimensions of pure silica particles. Assuming that our pure and mixed silica particles are compact agglomerates, which is the most reasonable assumption for our silica particles with fractal dimension of 2.54–2.55 close to the spherical particles with fractal dimension of 3, the surface and volume equivalent diameters become identical to the mobility diameter of these particles. The SMPS results showed that the particles generated from pure compounds resulted in unimodal size distributions, while the particles generated from mixtures were associated with bimodal size distributions. The first peak of the bimodal size distribution indicated that also the mixture generated some pure soluble particles. The size distributions allowed us to estimate the total soluble vs. insoluble mass fractions present in the mixed particle population.

CCN activity measurements were conducted in various supersaturations up to 1.5 %, and activation ratio curves were determined for the evaluated particles. Afterward, the experimental data were compared to theoretical values using adsorption theory (e.g. Sorjamaa and Laaksonen, 2007) for the pure silica particles, κ-Köhler-theory (Petters and Kreidenweis, 2007) for the pure soluble particles, and a model describing mixtures of soluble and insoluble components introduced by Kumar et al. (2011b). The CCN activation of pure soluble and insoluble particles was in good agreement with κ-Köhler theory and adsorption theory. For mixed particles, however, the observed critical supersaturations were higher than those expected from the model by Kumar et al. (2011b), if constant soluble and insoluble mass fractions were assumed for the whole mixed particle population. This indicates that the particles were less hygroscopic than expected, indicating an uneven distribution of the soluble material in the aerosol size distribution. As the calculations were governed by the soluble mass (volume) fraction in the particles instead of adsorption effects, we could use the experimental critical supersaturations to estimate size-dependent distribution of the soluble material in the mixed particles. For particles > 150 nm in mobility diameter the soluble fractions were smaller and for particles < 150 nm mostly larger than in the total mixed particle population – indicating that the soluble material preferentially accumulated to particles < 150 nm, independent of the exact identity of the soluble species. If the uneven distribution of the soluble material was accounted for, the framework by Kumar et al. (2011b) could be successfully used to describe the CCN activation of insoluble particles mixed with soluble pollutants.

Our results indicate that knowing the fraction of soluble material (instead of the adsorption properties of the surfaces) is the key prerequisite for describing the CCN activation of silica mixed with soluble pollutants – at least for the relatively large soluble fractions studied here. Furthermore, our results indicate that well-defined descriptions of the coating processes are crucial for elucidating the phenomena governing the CCN activation of insoluble particles mixed with soluble compounds. We also conclude that although the model by Kumar et al. (2011b) was originally introduced for fresh dust coated by a layer of soluble salt after ageing, it gives a reasonable estimate of the potential importance of adsorption

as compared with the bulk solubility of the mixed soluble–insoluble particles.

Acknowledgements. Financial support from the Nordic Centre of Excellence CRAICC (Cryosphere-atmosphere interactions in a changing Arctic climate), Vetenskapprådet (grant no. 2011-5120), Academy of Finland (272041, 259005, 283031 and 138951) and the European Research Council (StG no. 27877 ATMOGAIN and 335478 QAPPA) is gratefully acknowledged.

Edited by: S. M. Noe

References

Albrecht, B. A.: Aerosols, cloud microphysics, and fractional cloudiness, Science, 245, 1227–1230, 1989.

Biskos, G., Russell, L. M., Buseck, P. R., and Martin, S. T.: Nanosize effect on the hygroscopic growth factor of aerosol particles, Geophys. Res. Lett., 33, L07801, doi:10.1029/2005GL025199, 2006.

Boldridge, D.: Morphological characterization of fumed silica aggregates, Aerosol Sci. Technol., 44, 182–186, doi:10.1080/02786820903499462, 2010.

DeCarlo, P. F., Slowik, J. G., Worsnop, D. R., Davidovits, P., and Jimenez, J. L.: Particle morphology and density characterization by combined mobility and aerodynamic diameter measurements. Part 1: theory, Aerosol Sci. Technol., 38, 1185–1205, doi:10.1080/027868290903907, 2004.

Dusek, U., Reischl, G. P., and Hitzenberger, R.: CCN activation of pure and coated carbon black particles, Environ. Sci. Technol., 40, 1223–1230, 2006.

Fuchs, N. A.: The mechanics of aerosols, Pergamon Press, London, 1964.

Garland, J. A.: Condensation on ammonium sulphate paticles and its effect on visibility, Atmos. Environ., 3, 347–354, 1969.

Grayson, M., Ed.: Encyclopedia of glass, ceramics and cement, John Wiley & Sons, Inc, New york., 1985.

Haynes, W. M., Bruno, T. J., and Lide, D. R., Eds.: CRC handbook of chemistry and physics, 94th ed., CRC Press, available at: http://www.hbcpnetbase.com/, last access: 19 July 2013, 2013.

Haywood, J. and Boucher, O.: Estimates of the direct and indirect radiative forcing due to tropospheric aerosols: A review, Rev. Geophys., 38, 513–543, 2000.

Henning, S., Wex, H., Hennig, T., Kiselev, a., Snider, J. R., Rose, D., Dusek, U., Frank, G. P., Pöschl, U., Kristensson, A., Bilde, M., Tillmann, R., Kiendler-Scharr, a., Mentel, T. F., Walter, S., Schneider, J., Wennrich, C., and Stratmann, F.: Soluble mass, hygroscopic growth, and droplet activation of coated soot particles during LACIS Experiment in November (LExNo), J. Geophys. Res., 115, D11206, doi:10.1029/2009JD012626, 2010.

Hinds, W. C.: Aerosol technology: properties, behavior, and measurement of airborne particles, 2 Edn., John Wiley & Sons Inc., New York, 1999.

Hings, S. S., Wrobel, W. C., Cross, E. S., Worsnop, D. R., Davidovits, P., and Onasch, T. B.: CCN activation experiments with adipic acid: effect of particle phase and adipic acid coatings on soluble and insoluble particles, Atmos. Chem. Phys., 8, 3735–3748, doi:10.5194/acp-8-3735-2008, 2008.

Hiranuma, N., Kohn, M., Pekour, M. S., Nelson, D. a, Shilling, J. E., and Cziczo, D. J.: Droplet activation, separation, and compositional analysis: laboratory studies and atmospheric measurements, Atmos. Meas. Tech., 4, 2333–2343, doi:10.5194/amt-4-2333-2011, 2011.

Ibaseta, N. and Biscans, B.: Fractal dimension of fumed silica: Comparison of light scattering and electron microscope methods, Powder Technol., 203, 206–210, doi:10.1016/j.powtec.2010.05.010, 2010.

IPCC: (Intergovernmental Panel on Climate Change): Climate Change 2013, The Physical Science Basis, Cambridge University Press, Cambridge, 2013.

Jacob, D. J.: Introduction to atmospheric chemistry, Princeton University Press, Princeton, available at: http://www.ncbi.nlm.nih.gov/pubmed/14664619, 1999.

Jeyachandran, Y. L., Mielczarski, J. A, Mielczarski, E., and Rai, B.: Efficiency of blocking of non-specific interaction of different proteins by BSA adsorbed on hydrophobic and hydrophilic surfaces, J. Colloid Interface Sci., 341, 136–42, doi:10.1016/j.jcis.2009.09.007, 2010.

Kelly, W. P. and McMurry, P. H.: Measurement of particle density by inertial classification of Differential Mobility Analyzer-generated monodisperse aerosols, Aerosol Sci. Technol., 17, 199–212, 1992.

Keskinen, H., Romakkaniemi, S., Jaatinen, A., Miettinen, P., Saukko, E., Jorma, J., Mäkelä, J. M., Virtanen, A., Smith, J. N., and Laaksonen, A.: On-line characterization of morphology and water adsorption on fumed silica nanoparticles, Aerosol Sci. Technol., 45, 1441–1447, doi:10.1080/02786826.2011.597459, 2011.

Kiselev, a., Wennrich, C., Stratmann, F., Wex, H., Henning, S., Mentel, T. F., Kiendler-Scharr, a., Schneider, J., Walter, S., and Lieberwirth, I.: Morphological characterization of soot aerosol particles during LACIS Experiment in November (LExNo), J. Geophys. Res., 115, D11204, doi:10.1029/2009JD012635, 2010.

Kreidenweis, S. M., Koehler, K., DeMott, P. J., Prenni, A. J., Carrico, C., and Ervens, B.: Water activity and activation diameters from hygroscopicity data – Part I: Theory and application to inorganic salts, Atmos. Chem. Phys., 5, 1357–1370, doi:10.5194/acp-5-1357-2005, 2005.

Kulkarni, P., Baron, P. A., and Willeke, K., Ed.: Aerosol measurement: principles, techniques, and applications, 3 Edn., John Wiley & Sons, Inc., Hoboken, New Jersey, 2011.

Kumar, P., Sokolik, I. N., and Nenes, A.: Parameterization of cloud droplet formation for global and regional models: including adsorption activation from insoluble CCN, Atmos. Chem. Phys., 9, 2517–2532, doi:10.5194/acp-9-2517-2009, 2009.

Kumar, P., Sokolik, I. N., and Nenes, A.: Measurements of cloud condensation nuclei activity and droplet activation kinetics of fresh unprocessed regional dust samples and minerals, Atmos. Chem. Phys., 11, 3527–3541, doi:10.5194/acp-11-3527-2011, 2011a.

Kumar, P., Sokolik, I. N., and Nenes, A.: Cloud condensation nuclei activity and droplet activation kinetics of wet processed regional dust samples and minerals, Atmos. Chem. Phys., 11, 8661–8676, doi:10.5194/acp-11-8661-2011, 2011b.

Larsericsdotter, H., Oscarsson, S., and Buijs, J.: Structure, stability, and orientation of BSA adsorbed to silica., J. Colloid Interface Sci., 289, 26–35, doi:10.1016/j.jcis.2005.03.064, 2005.

Levin, E. L., Spector, P. E., Menon, S., Narayanan, L., and Cannon-Bowers, J. a: The effects of desert particles coated with sulfate on rain formation in the eastern Mediterranean, Hum. Perform., 9, 1511–1523, available at: http://www.tandfonline.com/doi/abs/10.1207/s15327043hup0901_1, 1996.

Liu, Q., Ma, X., and Zachariah, M. R.: Combined on-line differential mobility and particle mass analysis for determination of size resolved particle density and microstructure evolution, Microporous Mesoporous Mater., 153, 210–216, doi:10.1016/j.micromeso.2011.11.017, 2012.

Lohmann, U. and Feichter, J.: Global indirect aerosol effects: a review, Atmos. Chem. Phys., 5, 715–737, doi:10.5194/acp-5-715-2005, 2005.

Mackay, J. and Mensah, G. A.: Atlas of heart disease and stroke, World Health Organization (WHO), Geneva, 2004.

McCormick, R. A. and Ludwig, J. H.: Climate modification by atmospheric aerosols, Science, 156, 1358–1359, 1976.

McMurry, P. H., Wang, X., Park, K., and Ehara, K.: The relationship between mass and mobility foratmospheric particles: a new technique for measuring particle density, Aerosol Sci. Technol., 36, 227–238, doi:10.1080/027868202753504083, 2002.

Mikhailov, E., Vlasenko, S., Niessner, R., and Pöschl, U.: Interaction of aerosol particles composed of protein and saltswith water vapor: hygroscopic growth and microstructural rearrangement, Atmos. Chem. Phys., 4, 323–350, doi:10.5194/acp-4-323-2004, 2004.

Moore, R. H., Nenes, A., and Medina, J.: Scanning Mobility CCN Analysis – A method for fast measurements of size-resolved CCN distributions and activation kinetics, Aerosol Sci. Technol., 44, 861–871, doi:10.1080/02786826.2010.498715, 2010.

Park, K., Cao, F., Kittelson, D. B., and McMurry, P. H.: Relationship between particle mass and mobility for diesel exhaust particles., Environ. Sci. Technol., 37, 577–83, available at: http://www.ncbi.nlm.nih.gov/pubmed/12630475, 2003a.

Park, K., Kittelson, D. B., and McMurry, P. H.: A closure study of aerosol mass concentration measurements: comparison of values obtained with filters and by direct measurements of mass distributions, Atmos. Environ., 37, 1223–1230, doi:10.1016/S1352-2310(02)01016-6, 2003b.

Petters, M. D. and Kreidenweis, S. M.: A single parameter representation of hygroscopic growth and cloud condensation nucleus activity, Atmos. Chem. Phys., 7, 1961–1971, doi:10.5194/acp-7-1961-2007, 2007.

Pope, C. A. and Dockery, D. W.: Health effects of fine particulate air pollution?: lines that connect, J. Air Waste Manage. Assoc., 56, 709–742, 2006.

Pope, C. A., Ezzati, M., and Dockery, D. W.: Fine-particulate air pollution and life expectancy in the United States, N. Engl. J. Med., 360, 376–386, 2009.

Ramanathan, V., Crutzen, P. J., Kiehl, J. T., and Rosenfeld, D.: Aerosols, climate, and the hydrological cycle., Science, 294, 2119–2124, doi:10.1126/science.1064034, 2001.

Ravishankara, A. D.: Heterogeneous and multiphase chemistry in the troposphere, Science, 276, 1058–1065, 1997.

Roberts, G. and Nenes, A.: A continuous-flow streamwise thermal-gradient CCN chamber for atmospheric measurements, Aerosol Sci. Technol., 39, 206–221, doi:10.1080/027868290913988, 2005.

Rosenorn, T., Kiss, G., and Bilde, M.: Cloud droplet activation of saccharides and levoglucosan particles, Atmos. Environ., 40, 1794–1802, doi:10.1016/j.atmosenv.2005.11.024, 2006.

Ruehl, C. R., Chuang, P. Y., and Nenes, A.: Aerosol hygroscopicity at high (99 to 100 %) relative humidities, Atmos. Chem. Phys., 10, 1329–1344, doi:10.5194/acp-10-1329-2010, 2010.

Saathoff, H., Naumann, K.-H., Schnaiter, M., Schöck, W., Möhler, O., Schurath, U., Weingartner, E., Gysel, M., and Baltensperger, U.: Coating of soot and $(NH_4)_2SO_4$ particles by ozonolysis products of α-pinene, J. Aerosol Sci., 34, 1297–1321, doi:10.1016/S0021-8502(03)00364-1, 2003.

Scheckman, J. H., McMurry, P. H., and Pratsinis, S. E.: Rapid characterization of agglomerate aerosols by in situ mass-mobility measurements, Langmuir, 25, 8248–8254, doi:10.1021/la900441e, 2009.

Seinfeld, J. H. and Pandis, S. N.: Atmospheric Chemistry and Physics: From Air Pollution to Climate Change, 2nd Edn., 2006.

Shiraiwa, M., Ammann, M., Koop, T., and Pöschl, U.: Gas uptake and chemical aging of semisolid organic aerosol particles, P. Natl. Acad. Sci. USA, 108, 11003–11008, doi:10.1073/pnas.1103045108, 2011.

Skillas, G., Kunzel, S., Burtscher, H., Baltensperger, U., and Siegmann, K.: High fractal-like dimension of diesel soot agglomorates, J. Aerosol Sci., 29, 411–419, 1998.

Skillas, G., Burtscher, H., Siegmann, K., and Baltensperger, U.: Density and fractal-like dimension of particles from a laminar diffusion flame, J. Colloid Interface Sci., 217, 269–274, doi:10.1006/jcis.1999.6370, 1999.

Sorjamaa, R. and Laaksonen, A.: The effect of H_2O adsorption on cloud drop activation of insoluble particles: a theoretical framework, Atmos. Chem. Phys., 7, 6175–6180, doi:10.5194/acp-7-6175-2007, 2007.

Stratmann, F., Bilde, M., Dusek, U., Frank, G. P., Hennig, T., Henning, S., Kiendler-Scharr, A., Kiselev, A., Kristensson, A., Lieberwirth, I., Mentel, T. F., Pöschl, U., Rose, D., Schneider, J., Snider, J. R., Tillmann, R., Walter, S., and Wex, H.: Examination of laboratory-generated coated soot particles: an overview of the LACIS Experiment in November (LExNo) campaign, J. Geophys. Res., 115, D11203, doi:10.1029/2009JD012628, 2010.

Sugio, S., Kashima, A., Mochizuki, S., Noda, M., and Kobayashi, K.: Crystal structure of human serum albumin at 2.5 A resolution, Protein Eng., 12, 439–446, 1999.

Twomey, S.: Pollution and the planetary albedo, Atmos. Environ., 8, 1251–1256, 1974.

Virtanen, A., Ristimäki, J., and Keskinen, J.: Method for measuring effective density and fractal dimension of aerosol agglomerates, Aerosol Sci. Technol., 38, 437–446, doi:10.1080/02786820490445155, 2004.